Journal of Solid State Chemistry 249 (2017) 58–63

Contents lists available at ScienceDirect

Journal of Solid State Chemistry

journal homepage: www.elsevier.com/locate/jssc

Effect of Er^{3+} ions on the phase formation and properties of In_2O_3nanostructures crystallized upon microwave heating

Samantha C.S. Lemos[a], Fernanda C. Romeiro[a], Leonardo F. de Paula[a], Rosana F. Gonçalves[b], Ana P. de Moura[c], Mateus M. Ferrer[d], Elson Longo[d], Antonio Otavio T. Patrocinio[a], Renata C. Lima[a,*]

[a] Instituto de Química, Universidade Federal de Uberlândia, 38400-902 Uberlândia, MG, Brazil
[b] UNIFESP, Universidade Federal de São Paulo, 09972-270 Diadema, SP, Brazil
[c] LIEC, Instituto de Química, Universidade Estadual Paulista, 14800-900 Araraquara, SP, Brazil
[d] INCTMN-UFSCar, Universidade Federal de São Carlos, 13565-905 São Carlos, SP, Brazil

ARTICLE INFO

Keywords:
Indium oxide
Earth rare
Microwave hydrothermal
Photoluminescence
Photocatalyst

ABSTRACT

Regular sized nanostructures of indium oxide (In_2O_3) were homogeneously grown using a facile route, i.e. a microwave-hydrothermal method combined with rapid thermal treatment in a microwave oven. The presence of Er^{3+} doping plays an important role in controlling the formation of cubic (bcc) and rhombohedral (rh) In_2O_3 phases. The samples presented broad photoluminescent emission bands in the green-orange region, which were attributed to the recombination of electrons at oxygen vacancies. The photocatalytic activities of pure bcc-In_2O_3 and a bcc-rh-In_2O_3 mixture towards the UVA degradation of methylene blue (MB) were also evaluated. The results showed that Er^{+3} doped In_2O_3 exhibited the highest photocatalytic activity with a photonic efficiency three times higher than the pure oxide. The improved performance was attributed to the higher surface area, the greater concentration of electron traps due the presence of the dopant and the possible formation of heterojunctions between the cubic and rhombohedral phases.

1. Introduction

Indium oxide has stimulated great research interest due to its unique optical properties and advantages such as high specific area and applications in microelectronics [1,2]. This compound is an important n-type white semiconductor with a wide band gap (E_g=3.55–3.75 eV) and has been used in various applications such as optoelectronic devices, solar cells and photocatalysis [3–5]. The stable form of In_2O_3 has a body-centered cubic structure (bcc-In_2O_3), while the metastable corundum-type structure of In_2O_3 has a rhombohedral structure (rh-In_2O_3). The stabilization of the metastable In_2O_3 phase has been associated with the conversion of bcc-In_2O_3 at high pressures and temperatures [6,7]. The different activities of In_2O_3 are related to its crystalline phase and morphology, so there is interest in controlling these parameters. Li et al. [8] showed that sensors based on a mixture of cubic and rhombohedral structures exhibit better responses to NO_2 than the pure cubic oxide. Excellent photocatalytic activities for dye degradation under UV irradiation using hollow In_2O_3 nanocrystals were reported by Yin et al. [9] Additionally, Liu et al. showed that the rh-In_2O_3 phase exhibits higher photocatalytic activity than c-In_2O_3 for phenol degradation [10].

In_2O_3 materials have been prepared by solvothermal [11], sol-gel [12], microemulsion [13], and the hydrothermal methods [14] followed by heating in a conventional oven at high temperatures and long annealing times. The preparation of In_2O_3 nanostructures by a simple method under mild conditions of low temperature and short synthesis time is not common. The hydrothermal method combined with microwave heating is an environmentally friendly route for synthesizing the precursors of this oxide [15]. The use of microwave radiation in the hydrothermal system, introduced by Komarneni et al. [16] allows for the homogeneous formation of materials with excellent control of particle size with reduced preparation times [17,18]. We report in a previous work [19], the preparation of In_2O_3 microcrystals obtained by the calcination of $In(OH)_3$ microstructures in a microwave oven. Annealing in a microwave oven requires lower temperatures and shorter calcination times [20,21]. However, its use to obtain In_2O_3 materials has been poorly explored.

Herein, we report the synthesis of pure and Er^{3+} doped In_2O_3 nanostructures using a facile microwave-hydrothermal method combined with rapid heating of as-prepared $In(OH)_3$-InOOH precursors at

* Corresponding author.
E-mail address: rclima@ufu.br (R.C. Lima).

http://dx.doi.org/10.1016/j.jssc.2017.02.011
Received 6 October 2016; Received in revised form 10 February 2017; Accepted 11 February 2017
Available online 14 February 2017

350 °C for 2 min in a microwave oven. The results show that Er^{3+} ions doping was fundamental to stabilizing the crystalline rhombohedral phase, which affected the photocatalytic activity. Rapid annealing using a microwave oven allowed for obtaining highly crystalline particles with a desirable shape and size.

2. Materials and methods

2.1. Synthesis of In_2O_3

The precursors were obtained from the addition of 14.40 mL $In(NO_3)_3$ (0.10 mol L^{-1}) and 2.00 mL PEG 200 in 40 mL of distilled water under constant stirring. The pH was adjusted to 9.70 using a KOH aqueous solution. To prepare the doped precursor, a stoichiometric amount of a 3 mol L^{-1} $Er(NO_3)_3$ solution was added to the mixture in order to reach 4.0 mol% of Er^{3+} in relation to In^{3+} ions. The final solution was transferred into an autoclave, and then sealed and placed in the microwave-hydrothermal equipment. The solutions were heated at 140 °C for 2 min. The precipitate powder was washed several times with deionized water and ethanol and dried in an air atmosphere. The as-prepared $In(OH)_3$-InOOH and Er^{3+} doped $In(OH)_3$-InOOH precursors were annealed at 350 °C for 2 min in a microwave oven to obtain In_2O_3 nanostructures.

2.2. Materials characterization

$In_{2-x}Er_xO_3$ samples were characterized by X-ray diffraction (Shimadzu XRD 6000) using Cu Kα as the radiation source. The structure was refined using the Rietveld Method and the General Structure Analysis System (GSAS) package, with the EXPGUI graphical user interface [22]. The morphological characterization was performed using a field emission scanning electron microscope (FE-SEM, Zeiss Supra35) operating at 5 kV. Transmission electron microscopy (TEM) was performed on an FEI Tecnai G2F20, operating at 200 kV. UV–visible spectra of $In_{2-x}Er_xO_3$ samples were obtained on a Cary 5 G spectrophotometer in the 200–900 nm region. Raman spectra at room temperature were recorded on an RFS/100/S Bruker FT-Raman spectrometer, with an Nd: YAG laser providing an excitation light at 1064 nm and a spectral resolution of 4 cm^{-1}. Photoluminescence (PL) spectra were recorded at room temperature by a thermal Jarrel-Ash Monospec 27 monochromator and a Hamamatsu R446 photomultiplier (λ_{exc}=350.7 nm).

2.3. Photocatalytic studies

The photocatalytic tests were carried out in a round borosilicate glass reactor at 298 K. 100 mg L^{-1} of the photocatalysts were suspended in a 20 mL of a 2×10^{-5} mol L^{-1} methylene blue (MB^+) aqueous solution as previously described [23]. The system was stirred for 30 min in the dark in order to reach adsorption equilibrium. Afterwards, the reactor was irradiated for 150 min using a 150 W Xe lamp. A KG1 glass filter was employed to block photons with energies below 300 nm, while infrared radiation was cut off by a water filter. The photon flux (3.24×10^{15} quanta s^{-1}) was measured by chemical actinometry using potassium tris(oxalate)ferrate(III) [24,25]. The photonic efficiencies (ξ) were calculated as previously reported [26], using Eq. (1), in which r(MB^+) is the rate in molecules s^{-1} of methylene blue degradation, obtained spectrophotometrically, and I_0 is the photon flux. Control experiments were carried out in the absence of any photocatalyst to show the role of the samples on the photochemical reaction; these experiments revealed that less than 2% of the dye was bleached after 150 min of irradiation.

$$\xi = 100x\ r(MB^+)/I_0 \quad (1)$$

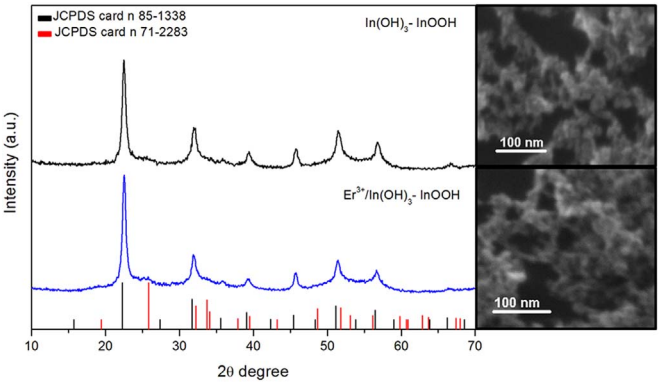

Fig. 1. XRD patterns and FE-SEM images of the as-synthesized pure and Er^{3+} doped $In(OH)_3$-InOOH precursors.

3. Results and discussion

3.1. Structural and microstructural characterization

Fig. 1 shows the XRD patterns and FE-SEM images of the as-prepared $In(OH)_3$-InOOH and Er^{3+} doped $In(OH)_3$-InOOH precursors obtained under microwave-hydrothermal conditions. The XRD patterns correspond to the cubic phase of $In(OH)_3$ with space group *Im-3* (JCPDS no. 85–1338) and lattice constant a=7.974 Å and orthorhombic structure of InOOH (space group *P21nm*) in agreement with the JCPDS file no. 71–2283 for both samples. Doped and undoped $In(OH)_3$-InOOH precursors prepared under mild conditions formed particle agglomerates with irregular shapes and a size of about 10 nm, as shown in the micrographs.

Fig. 2 displays the XRD patterns refined by the Rietveld method of pure In_2O_3 and Er^{3+} doped In_2O_3 samples obtained after annealing the as-prepared $In(OH)_3$-InOOH precursors at 350 °C for 2 min in a microwave oven. The diffraction peaks of pure In_2O_3 sample can be indexed to a cubic lattice of In_2O_3 (JCPDS no. 06–0416) with space group $Ia\bar{3}$. The Er^{3+} doped In_2O_3 sample presented a peak in the region of 2θ =32.63° related to the rhombohedral structure (space group $R\bar{3}c$ of In_2O_3) according to the JCPDS data card no. 72–0683. Table 1 shows the values of the profile and lattice parameters obtained after the final refinement cycle. The low values of χ^2 and profile parameters (R_p, R_{wp}) indicate a high quality of refinement. The value of the cell parameter *a* of both samples are similar. However, the presence of the dopant influenced phase formation, wherein the pure bcc-In_2O_3 was transformed into a mixture of bcc-In_2O_3 and rh-In_2O_3. Rietveld refinement of the XRD patterns of the doped Er^{3+} doped In_2O_3 sample showed the presence of 87.3% bcc-In_2O_3 phase and 12.7% rh-In_2O_3

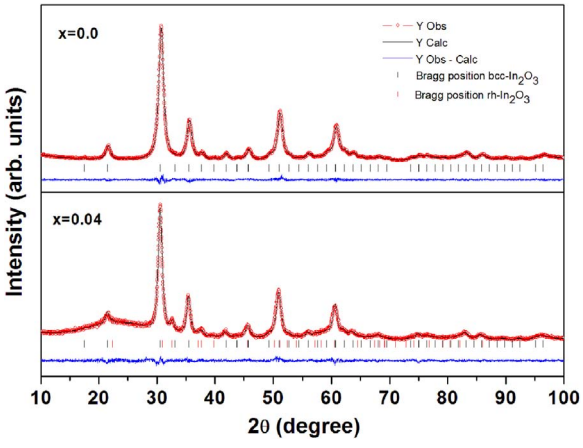

Fig. 2. XRD patterns after structural refinement procedure using Rietveld method for the $In_{2-x}Er_xO_3$ nanostructures, x= mol of Er^{3+} ions.

Table 1
Quality scores refinement and parameters obtained by Rietveld method for the $In_{2-x}Er_xO_3$ samples (x= mol of Er^{3+} ions).

Samples	bcc-In_2O_3 cell parameters a=b=c (Å)	rh-In_2O_3 cell parameters		R_{wp} (%)	R_p (%)	R_{bragg} (%)	χ^2
		a=b (Å)	c (Å)				
x= 0.0	10.1110(3)	–	–	6.23	4.65	1.09	1.91
x= 0.04	10.1504(7)	5.531 (14)	14.621 (43)	5.81	4.51	2.05	1.38

phase, with cell parameters for rh-In_2O_3 of a= b=5.5314 Å and c=14.6212 Å.

The representative crystal structures of the bcc-rh-In_2O_3 mixture obtained by Rietveld refinement using the Crystal Maker Program for Windows are shown in Fig. 3. The phase bcc-In_2O_3 consists of two types of In^{3+} ions surrounded by oxygen anions in the octahedral (1) and trigonal prismatic (2) coordinations, while rh-In_2O_3 is formed when the In^{3+} ions are surrounded by oxygen anions in a trigonal biprism coordination [27]. The mixture of these two structures obtained under rapid heating in the microwave oven is due to the addition of Er^{3+} ions into the oxide lattice. These ions, under certain synthesis conditions, can change the growth rate in the crystal plane of cubic In_2O_3, promoting the formation of the rhombohedra arrangement, as observed by Li et al. in Zn doped In_2O_3 samples [8]. Kim et al. [28] reported that the rh-In_2O_3 phase can be thermally stabilized by Eu^{3+} doping due to an increase in adsorption enthalpy between the Eu^{3+} ions and the host oxygen anions.

The morphology of the In_2O_3 powders obtained from the annealing of as-prepared $In(OH)_3$-InOOH precursors was studied by FE-SEM and TEM, as shown in Fig. 4. The micrographs show that the pure In_2O_3 and Er^{3+} doped In_2O_3 samples consisted of agglomerated particles (Fig. 4(a,c)). Microwave heating is an efficient method for the formation of crystalline In_2O_3 and is faster when compared to conventional, prolonged calcination [29,30]. In the rapid 2 min of annealing in the microwave oven, the sample is directly heated and the crystallization of the material is accelerated, which inhibit particles growth and allows for the nanometer size of $In(OH)_3$-InOOH precursors.

A careful analysis of the TEM images showed a difference in the morphology of the pure and doped samples (Fig. 4(b,d)). The pure In_2O_3 presented irregular rounded shapes (Fig. 4(b)). On the other hand, the Er^{3+} doped In_2O_3 sample revealed faces tending to a cube morphology (Fig. 4(d)). The calculated particle sizes were about 10 and 14 nm for pure and Er^{3+} doped In_2O_3 samples, respectively. The selected area electron diffraction (SAED) patterns of the samples, shown in Fig. 4 (inset), exhibit spotty rings are indexed as (222), (400), (440), and (622) reflections of the bcc-In_2O_3, which are consistent with the XRD results in Fig. 2. A strong ring pattern due to (110) reflection from the rhombohedral structure was identified in the SAED patterns of the doped sample. Thus, the SAED patterns also indicated the polycrystalline nature of the In_2O_3 samples.

The surface parameters obtained from the N_2-sorption data are given in Table 2. The specific surface area of Er^{3+} doped In_2O_3 was two times higher than the surface area of pure In_2O_3. A large surface area has a positive effect on the photocatalytic behavior since more surface active sites are available, increasing the adsorption of reactants. The higher surface area of Er^{3+}-In_2O_3 was accompanied by a greater pore volume.

According to the surface energies calculated by Walsh and Catlow [31], it is possible to generate a Wulff construction of the ideal structure of In_2O_3. Fig. 5 shows the energies and morphology obtained for In_2O_3.

From the ideal structure of In_2O_3, it is possible to modulate the surface energies to find the morphology obtained experimentally. In this way, the cubic shape was achieved when there was stabilization of the (100) surface. Therefore, it is possible to obtain the surface energy rate between the surfaces in order to achieve cubic faceting.

The Wulff crystal modulation allowed us to know the relation between the surfaces in order to obtain the experimental morphology. In many cases, the ideal structures are not in agreement with the experimental results for several reasons, such as the method of synthesis, impurities and additives [32]. The calculations allow us to conclude that the incorporation of Er^{3+} ions in the matrix resulted in a smaller surface energy of (100) than the other surfaces to a point where its formation prevailed.

The UV–visible spectra of the pure In_2O_3 and Er^{3+} doped In_2O_3 powders are shown in Fig. 6(a). Absorption peaks located at 490, 521, 546 and 653 nm correspond to the transitions in the $4f^{11}$ shell of the Er^{3+} ion: $^4I_{15/2} \rightarrow {}^4F_{7/2}$, $^4I_{15/2} \rightarrow {}^2H_{11/2}$, $^4I_{15/2} \rightarrow {}^4S_{3/2}$ and $^4I_{15/2} \rightarrow {}^4F_{9/2}$, respectively [1,33], indicating the presence of Er^{3+} ions into the In_2O_3 lattice. The band gap energy values determined by the Kubelka Munk function [34] were 2.8 and 3.0 eV for pure In_2O_3 and Er^{3+} doped In_2O_3 (Fig. 6(a) inset), respectively, which are consistent with the findings of King et al. [35]. For comparison, the absorption spectra of the powder suspensions at the same concentration and under conditions similar to those employed in the photocatalytic tests are shown in Fig. S1 (Supplementary material). Under these conditions, it is not possible to observe the characteristic absorption peaks of Er^{3+}, probably due to the light scattering.

The Raman measurements of In_2O_3 samples ranging from 100 to 700 cm^{-1} are shown in Fig. 6(b). The Raman spectrum of the pure In_2O_3 sample displays peaks characteristic of the vibration modes of body centered cubic oxide [36,37]. Signals at 131, 306 and 366 cm^{-1} are related to In-O (vibration of InO_6 structure units), bending

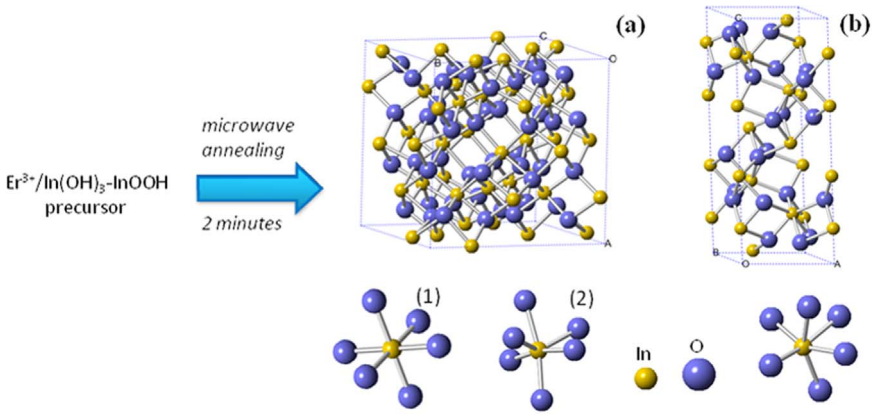

Fig. 3. Crystal structures obtained by Rietveld refinement from XRD patterns of the Er^{3+} doped In_2O_3 sample (a) cubic phase and (b) rhombohedral phase.

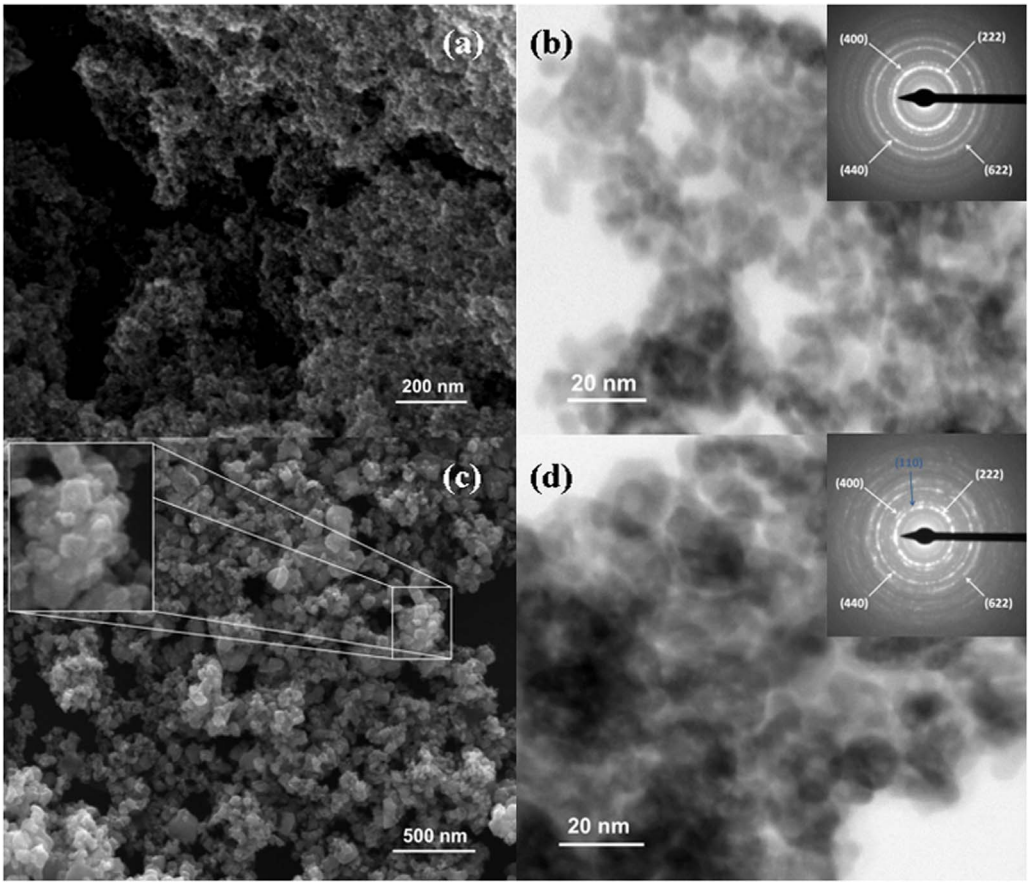

Fig. 4. FE-SEM and TEM images of $In_{2-x}Er_xO_3$ nanostructures, x= mol of Er^{3+} ions (a-b) x=0.0 and (c–d) x=0.04. The inset shows the SAED patterns.

Table 2
Surface parameters for the $In_{2-x}Er_xO_3$ samples obtained by N_2 adsorption/desorption isotherms (x= mol of Er^{3+} ions).

Samples	Surface area (m^2/g)	Volume of pores (cm^3/g)	Pore diameter (nm)
x= 0.0	111.19	0.49	13.29
x=0.04	235.73	0.92	9.76

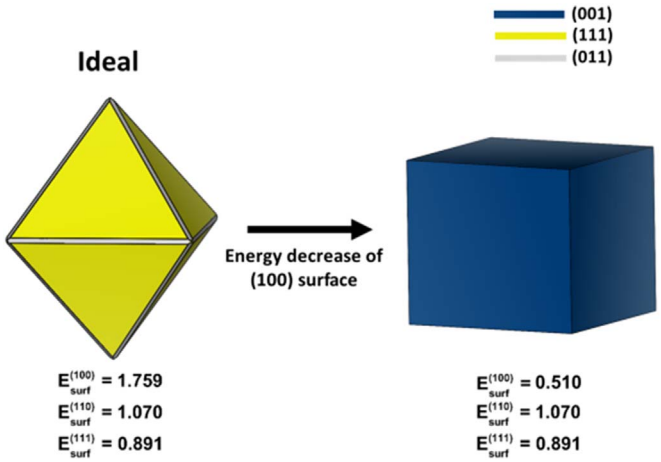

Fig. 5. Wulff Crystals of In_2O_3.

vibration of $\delta(InO_6)$ octahedron and stretching vibrations of In-O-In, respectively. The peaks at 494 and 627 cm^{-1} are assigned to the stretching vibrations of the same $\upsilon(InO_6)$ octahedrons. The Raman modes of Er^{3+} doped In_2O_3 shows peaks at 162 and 220 cm^{-1}, attributed to the $A_{1\,g}$ and E_g modes of rh-In_2O_3 [9], respectively, and confirm the presence of a bcc-rh-In_2O_3 mixture. The substitutional doping sites allow the formation of metastable rh-In_2O_3 structure and stabilization of the bcc-rh-In_2O_3 mixture at the Er^{3+} ions concentration used. The results found here are in agreement with those reported by Farvid et al. [38] that showed the influence of Cr^{3+} ions on the In_2O_3 crystal growth and stability of cubic and metastable rhombohedral phases of oxide.

The photoluminescence (PL) spectra of the $In_{2-x}Er_xO_3$ samples under 350 nm excitation are shown in Fig. 7. Broad PL emission bands in the green-orange region were observed for both samples, which can be ascribed to the recombination of electrons on ionized oxygen vacancies and holes in the valence band, as previously observed by Jean et al. [39] in In_2O_3 nanotowers. The visible emissions of In_2O_3 nanostructures have been observed in multiple studies. Jeong et al. [40] synthesized In_2O_3 nanobelts that exhibited a broad emission at 570 nm and a shoulder at 630 nm related to oxygen vacancies. A strong PL emission in the blue-green region of In_2O_3 column and pyramid structures was observed by Guha et al. [41] attributed to oxygen vacancies and indium-oxygen vacancy centers. Kumar et al. [42] showed by EPR that indium interstitials play an important role in the photoluminescent properties of In_2O_3 octahedron structures.

Fig. 7(b,c) displays the PL curves of pure and doped In_2O_3 deconvoluted using Gaussian fittings: blue (P1 at 469 nm), green (P2 at 545 nm), orange (P3 at 618 nm) and two red components (P4 and P5 at 697 nm and 788 nm, respectively). The areas under each curve, shown in Table 3, indicate different defects generated, in which the P1 and P2 emission peaks are commonly attributed to deep-level or trapped emissions states caused by oxygen vacancies [43]. Symmetry breaking induced by vacancies in the lattice can lead to the existence of intermediary energy levels within the forbidden band gap. Thus, it is believed that these vacancies play an important role in the formation of

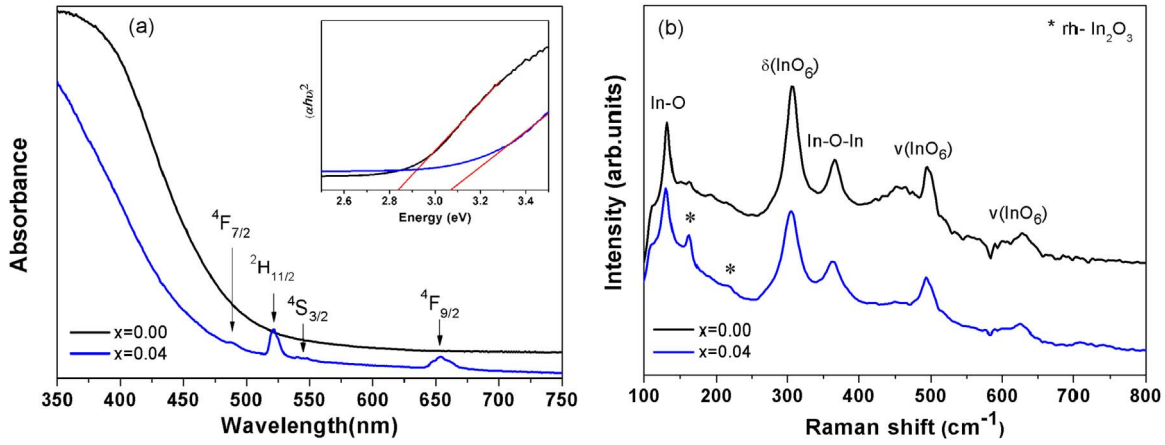

Fig. 6. Absorbance spectra (a) and Raman spectra (b) of $In_{2-x}Er_xO_3$ samples, x= mol of Er^{3+}. The inset of Figure (a) shows a plot of $(ahv)^2$ versus the energy of the samples.

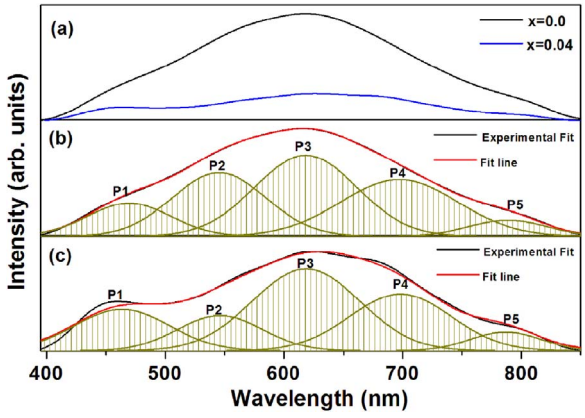

Fig. 7. Photoluminescence spectra of $In_{2-x}Er_xO_3$ samples, x= mol of Er^{3+}(a). Deconvoluted photoluminescence curves results (b) x=0.0 (c) x=0.04.

Table 3
Fitting parameters of the PL spectra of $In_{2-x}Er_xO_3$ nanostructures (x= mol of Er^{3+}).

$In_{2-x}Er_xO_3$	% area				
	P1	P2	P3	P4	P5
x= 0.0	11,1	24,0	33,2	26,7	5,0
x= 0.04	17,3	13,2	38,4	25,2	5,9

deep-level defects, influencing the green PL emission process in In_2O_3.

3.2. Photocatalytic activity

The photocatalytic activity of pure and Er^{3+} doped In_2O_3 was evaluated regarding the discoloration of methylene blue (MB^+) aqueous solutions, as shown in Fig. 8. Faster and more efficient degradation was observed with doped In_2O_3 in relation to that with the pure oxide. After 150 min, c.a. 20% of the dye was degraded by Er^{3+} doped In_2O_3, in contrast to only 5% observed for undoped In_2O_3. The discoloration of MB^+ in the presence of In_2O_3 photocatalysis can be fitted to the Langmuir-Hinshelwood kinetic model [44]. The observed discoloration rates for the doped and pure samples were, respectively, 1.5×10^{-3} and 0.5×10^{-3} min^{-1}. The calculated photonic efficiency was 1.4% and 0.5%, respectively for Er^{3+} doped In_2O_3 and pure In_2O_3. Even if the discoloration rates were normalized to the specific surface area, it is noteworthy to observe that the doped sample was almost two times more active than pure In_2O_3. This indicates that the improved performance is also related to electronic factors associated to the presence of the rhombohedral phase.

The photocatalytic efficiencies corroborate with the photoluminescence measurements that evidenced a high concentration of electrons traps in In_2O_3 doped with Er^{3+}. These trap states should decrease the electron/hole recombination rates and improve the charge transfer processes in the oxide surface and, consequently, lead to more efficient oxidation of the dye. Moreover, the results presented here are in agreement with the data obtained by Liu et al. [10] which show that rhombohedral In_2O_3 exhibits higher photocatalytic activity than the cubic polymorph. As evidenced by the XRD data, the introduction of the Er^{3+} dopant in the In_2O_3 matrix led to the stabilization of a mixture of the cubic and rhombohedral phases, which induced a higher concentration of oxygen vacancies. The presence of such as defects in the lattice structure favors photocatalytic activity, as extensively discussed for other semiconductor-based photocatalysts [23,45,46].

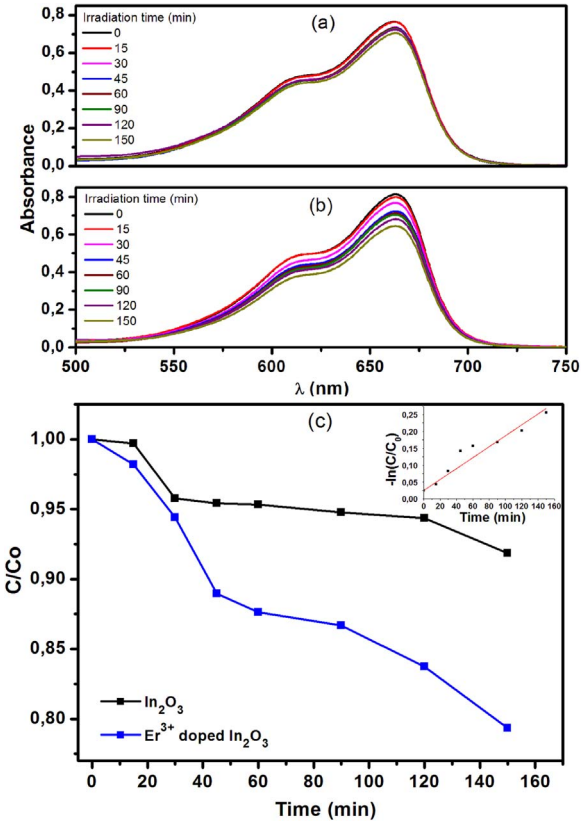

Fig. 8. UV–Vis spectral changes of MB^+ solutions under irradiation in the presence of $In_{2-x}Er_xO_3$ samples, x= mol of Er^{3+}(a) x=0.0 (b) x=0.04. (c) Normalized photodegradation curves as a function of irradiation time (I_0 =3.24×10^{15} quanta s^{-1}). *Inset:* Rate constant, k, (- ln C/C_0) x t.

Moreover, it is expected that the different crystalline phases have slightly different conduction band edge positions as observed for other semiconductors, eg. TiO_2 [45,47], which leads to formation of heterojunctions in the doped sample. In fact literature data indicate that the rh-In_2O_3 has c.a. 0.1–0.2 eV more positive conduction band edge than bcc-In_2O_3, which agrees well with the results presented here [48]. As a result, the electron/hole recombination is decreased in relation to the pure oxide. The improved photocatalytic activity evidences the positive influence of the microwave heating on the formation of heterojunction in polycrystalline materials.

4. Conclusions

In summary, pure In_2O_3 and Er^{3+} doped In_2O_3 nanostructures were synthesized successfully by annealing the as-synthesized $In(OH)_3$-InOOH precursors at 350 °C for 2 min in a microwave oven. The rapid preparation via microwave led to the formation of crystalline nanoparticles of pure In_2O_3 and Er^{3+} doped In_2O_3 with similar sizes as that of their precursors. The samples presented broad photoluminescent emission, which can be attributed to the effect of oxygen deficiencies. The addition of Er^{3+} ions also favored the stabilization of the rhombohedra in the In_2O_3 phase, contributing to the cubic-rhombohedra In_2O_3 mixture, with a higher surface area and slower electron/hole recombination. As a result, improved photocatalytic activity was observed regarding methylene blue degradation for Er^{3+} doped In_2O_3 in relation to pure In_2O_3 with a cubic structure.

Acknowledgements

The authors are grateful to Coordenação de Aperfeiçoamento de Pessoal de Nível Superior (Capes), Conselho Nacional de Desenvolvimento Científico e Tecnológico (CNPq) and Fundação de Amparo à Pesquisa do Estado de Minas Gerais (FAPEMIG, under Grant no. APQ-00988-13) for the financial support. The authors are also thankful to the Grupo de Materiais Inorgânicos do Triângulo (GMIT) research group supported by FAPEMIG (APQ-00330-14). This work is a collaboration research project of members of the Rede Mineira de Química (RQ-MG) supported by FAPEMIG (Project: CEX – RED-00010–14).

Appendix A. Supporting information

Supplementary data associated with this article can be found in the online version at doi:10.1016/j.jssc.2017.02.011.

References

[1] G.N. Aliev, V.G. Golubev, A.A. Dukin, D.A. Kurdyukov, A.V. Medvedev, A.B. Pevtsov, L.M. Sorokin, J.L. Hutchison, Phys. Solid State 44 (2002) 2224.
[2] Q. Wang, K. Yu, F. Xu, J. Wu, Ye Xu, Z. Zhu, Mater. Lett. 62 (2008) 2710.
[3] R. Sharma, R.S. Mane, S.-K. Min, S.-H. Han, J. Alloys Compd. 479 (2009) 840.
[4] L.-Y. Chen, Y. Liang, Z.-D. Zhang, Eur. J. Inorg. Chem. (2009) 903.
[5] A.M.E. Raj, K.C. Lalithambika, V.S. Vidhya, G. Rajagopal, A. Thayumanavan, M. Jayachandran, C. Sanjeeviraja, Physica B 403 (2008) 544.
[6] R.D. Shannon, Solid State Commun. 4 (1966) 629.
[7] C.T. Prewitt, R.D. Shannon, D.B. Rogers, A.W. Sleight, Inorg. Chem. 8 (1969) 1985.
[8] P. Li, H. Fan, Y. Cai, M. Xu, C. Long, M. Li, S. Lei, X. Zou, RSC Adv. 4 (2014) 15161.
[9] J. Yin, H. Cao, Inorg. Chem. 51 (2012) 6529.
[10] G. Liu, D. Chen, X. Jiao, CrystEngComm 11 (2009) 1828.
[11] H. Yang, Z. Yang, H. Liang, L. Liu, J. Guo, Y. Yang, Mater. Lett. 64 (2010) 1418.
[12] Z.-X. Cheng, X.-B. Dong, Q.-Y. Pan, J.-c. Zhang, X.-W. Dong, Mater. Lett. 60 (2006) 3137.
[13] Z.L. Zhan, W.H. Song, D.G. Jiang, J. Colloid Interface Sci. 271 (2004) 366.
[14] X. Xu, D. Wang, W. Wang, P. Sun, J. Ma, X. Liang, Y. Sun, Y. Ma, G. Lu, Sens. Actuators B 171 (2012) 1066.
[15] F.V. Motta, R.C. Lima, A.P.A. Marques, M.S. Li, E.R. Leite, J.A. Varela, E. Longo, J. Alloys Compd. 497 (2010) L25.
[16] S. Komarneni, R. Roy, Q.H. Li, Mater. Res. Bull. 27 (1992) 1393.
[17] F.C. Romeiro, J.Z. Marinho, A.C.A. Silva, N.F. Cano, N.O. Dantas, R.C. Lima, J. Phys. Chem. C 117 (2013) 26222.
[18] F.C. Romeiro, J.Z. Marinho, S.C.S. Lemos, A.P. de Moura, P.G. Freire, L.E. da Silva, E. Longo, R.A.A. Munoz, R.C. Lima, J. Solid State Chem. 230 (2015) 343.
[19] F.V. Motta, R.C. Lima, A.P.A. Marques, E.R. Leite, J.A. Varela, E. Longo, Mater. Res. Bull. 45 (2010) 1703.
[20] A.Z. Simoes, M.A. Ramirez, C.S. Riccardi, E. Longo, J.A. Varela, Mater. Charact. 59 (2008) 675.
[21] J.Z. Marinho, R.H.O. Montes, A.P. de Moura, E. Longo, J.A. Varela, R.A.A. Munoz, R.C. Lima, Mater. Res. Bull. 49 (2014) 572.
[22] A.C. Larson, R.B.V. Dreele, Los Alamos national laboratory report LAUR 86, 2004.
[23] A.O.T. Patrocinio, J. Schneider, M.D. Franca, L.M. Santos, B.P. Caixeta, A.E.H. Machado, D.W. Bahnemann, RSC Adv. 5 (2015) 70536.
[24] C.G. Hatchard, C.A. Parker, Proc. R. Soc. Lond. A 235 (1956) 518.
[25] S. Goldstein, J. Rabani, J. Photochem. Photobiol. A 193 (2008) 50.
[26] A. Mills, C. Hill, P.K.J. Robertson, J. Photochem. Photobiol. A 237 (2012) 7.
[27] F. Fuchs, F. Bechstedt, Phys. Rev. B 77 (2008) 155107.
[28] W.J. Kim, B.-K. Min, D. Pradhan, Y. Sohn, CrystEngComm 17 (2015) 1189.
[29] D. Han, P. Song, H. Zhang, H. Yan, Q. Xu, Z. Yang, Q. Wang, RSC Adv. 4 (2014) 50241.
[30] J. Yang, C. Lin, Z. Wang, J. Lin, Inorg. Chem. 45 (2006) 8973.
[31] A. Walsh, C.R.A. Catlow, J. Mater. Chem. 20 (2010) 10438.
[32] J. Andres, L. Gracia, A.F. Gouveia, M.M. Ferrer, E. Longo, Nanotechnology 26 (2015) 405703.
[33] Z. Xu, J. Gong, W. Liu, K. Zhang, Q. Lu, Opt. Commun. 292 (2013) 135.
[34] P.M.-A. Kubelka, F. Zeit, Fur. Tech. Phys. 12 (1931) 593.
[35] P.D.C. King, T.D. Veal, F. Fuchs, C.Y. Wang, D.J. Payne, A. Bourlange, H. Zhang, G.R. Bell, V. Cimalla, O. Ambacher, R.G. Egdell, F. Bechstedt, C.F. McConville, Phys. Rev. B 79 (2009) 205211.
[36] T. Zhang, F. Gu, D. Han, Z. Wang, G. Guo, Sens. Actuators B 177 (2013) 1180.
[37] W. Yin, J. Su, M. Cao, C. Ni, S.G. Cloutier, Z. Huang, X. Ma, L. Ren, C. Hu, B. Wei, J. Phys. Chem. C 113 (2009) 19493.
[38] S.S. Farvid, M. Hegde, P.V. Radovanovic, Chem. Mater. 25 (2013) 233.
[39] S.-T. Jean, Y.-C. Her, Cryst. Growth Des. 10 (2010) 2104.
[40] J.S. Jeong, J.Y. Lee, C.J. Lee, S.J. An, G.C. Yi, Chem. Phys. Lett. 384 (2004) 246.
[41] P. Guha, S. Kar, S. Chaudhuri, Appl. Phys. Lett. 85 (2004) 3851.
[42] M. Kumar, V.N. Singh, F. Singh, K.V. Lakshmi, B.R. Mehta, J.P. Singh, Appl. Phys. Lett. 92 (2008) 171907.
[43] X.S. Peng, G.W. Meng, J. Zhang, X.F. Wang, Y.W. Wang, C.Z. Wang, L.D. Zhang, J. Mater. Chem. 12 (2002) 1602.
[44] A. Mills, C. O'Rourke, K. Moore, J. Photochem. Photobiol. A 310 (2015) 66.
[45] J. Schneider, M. Matsuoka, M. Takeuchi, J. Zhang, Y. Horiuchi, M. Anpo, D.W. Bahnemann, Chem. Rev. 114 (2014) 9919.
[46] X. Xin, T. Xu, J. Yin, L. Wang, C. Wang, Appl. Catal. B 176 (2015) 354.
[47] X.L. Wang, A. Kafizas, X.O. Li, S.J.A. Moniz, P.J.T. Reardon, J.W. Tang, I.P. Parkin, J.R. Durrant, J. Phys. Chem. C 119 (2015) 10439.
[48] J. Luo, X.S. Zhou, L. Ma, X.Y. Xu, H.T. Ruan, Z.B. Zhang, RSC Adv. 6 (2016) 52627.